ADVANCED FUNCTIONAL MATERIALS
www.afm-journal.de

Reversible Enhancement of Electronic Conduction Caused by Phase Transformation and Interfacial Segregation in an Entropy-Stabilized Oxide

*Hasti Vahidi, Alexander D. Dupuy, Benjamin X. Lam, Justin Cortez, Pulkit Garg, Timothy J. Rupert, Julie M. Schoenung, and William J. Bowman**

Entropy-stabilized oxide (ESO) research has primarily focused on discovering unprecedented structures, chemistries, and properties in the single-phase state. However, few studies discuss the impacts of entropy stabilization and secondary phases on functionality and in particular, electrical conductivity. To address this gap, electrical transport mechanisms in the canonical ESO rocksalt (Co,Cu,Mg,Ni,Zn)O are assessed as a function of secondary phase content. When single-phase, the oxide conducts electrons via Cu^{+}/Cu^{2+} small polarons. After 2 h of heat treatment, Cu-rich tenorite secondary phases form at some grain boundaries (GBs), enhancing grain interior electronic conductivity by tuning defect chemistry toward higher Cu^{+} carrier concentrations. 24 h of heat treatment yields Cu-rich tenorite at all GBs, followed by the formation of anisotropic Cu-rich tenorite and equiaxed Co-rich spinel secondary phases in grains, further enhancing grain interior electronic conductivity but slowing electronic transport across the tenorite-rich GBs. Across all samples, the total electrical conductivity increases (and decreases reversibly) by four orders of magnitude with heat-treatment-induced phase transformation by tuning the grains' defect chemistry toward higher carrier concentration and lower migration activation energy. This work demonstrates the potential to selectively grow secondary phases in ESO grains and at GBs, thereby tuning the electrical properties using microstructure design, nanoscale engineering, and heat treatment, paving the way to develop many novel materials.

1. Introduction

Utilizing configurational entropy as a driving force to stabilize single-phase solid solutions has enabled unprecedented functional materials[1–10] for energy storage/conversion and information technologies.[11–17] Entropy-stabilized oxides (ESOs) are a subset of high entropy oxides (HEOs)—themselves a subset of complex concentrated oxides (CCOs)—in which configurational entropy unambiguously governs the stabilization of a single-phase solid solution[18] containing (partially) immiscible constituents.[19] HEOs/ESOs' significant promise stems from the compositional complexity and short-range disorder, which offers unique distributions of oxygen–metal bond lengths, bond angles, vibrational frequencies, degree of covalence, and cation coordination numbers,[20] governing functional properties.[21,22] For example, the entropy-stabilized local disorder was recently shown to create overlapping site energy distributions, facilitating Li^{+} mobility through a percolating network[1] in an all-solid-state battery electrolyte.

Despite significant progress, charge transport mechanisms in HEOs/ESOs have not been elucidated given the complexity and many degrees of freedom, particularly for the undoped model systems. While Li-doped ESOs have attracted significant research attention to date, knowledge about transport mechanisms in undoped ESOs is necessary as it underpins the analysis of more complicated doped ESOs. For instance, it is still debated whether the Li-doped $(Co,Cu,Mg,Ni,Zn)_{1-x}Li_xO$ has reasonable electronic conductivity needed for applications including Li^{+} battery active electrode materials.[15,23]

Additionally, understanding the influence of phase transformations is necessary for elucidating functional properties due to the metastable nature of HEOs/ESOs (i.e., the temperature-dependent competition between entropic and enthalpic phase stabilization), as demonstrated by observed reversible phase transformation in ESOs.[8,18] Balcerzak et al.[24] observed three unique conductivity activation energies in the canonical undoped

H. Vahidi, A. D. Dupuy, B. X. Lam, J. Cortez, P. Garg, T. J. Rupert, J. M. Schoenung, W. J. Bowman
Department of Materials Science and Engineering
University of California
Irvine, CA 92697-2585, USA
E-mail: will.bowman@uci.edu

The ORCID identification number(s) for the author(s) of this article can be found under https://doi.org/10.1002/adfm.202315895

DOI: 10.1002/adfm.202315895

ESO (Co,Cu,Mg,Ni,Zn)O between 205–875 °C, which was attributed to reversible phase transformations based on lattice parameter changes measured by high-temperature X-ray diffraction (XRD) and phase separation caused by low compatibility of Zn^{2+} and Cu^{2+} with other elements. However, a comprehensive understanding of this phenomenon is lacking due to the absence of direct high-spatial-resolution microstructural evidence. Previous XRD results prove that reversible entropic phase transformations can be engineered by varying heat treatment conditions to tune the phase state between the enthalpy-dominated multiphase state (comprising Cu-rich tenorite and Co-rich spinel) and the entropy-dominated single-phase state.[8,18,25,26] Nonetheless, there are currently no publications explaining how changes in crystal structure, microstructure, and composition influence charge transport and secondary phase particle morphology as an ESO undergoes phase transformations. Moreover, the structure and composition of interfaces such as grain boundaries (GBs) and heterointerfaces (HIs) and their connection with electrical conductivity, as a function of phase transformation, remains unexplored despite the fact that interfacial conductivity is significant for engineering ESO solid electrolytes[27] and thin film transistors.[28]

Here, we elucidate the effect of heat-treatment-induced phase transformations on the electrical conductivity of polycrystalline (Co,Cu,Mg,Ni,Zn)O ESO using direct atomic- and nanoscale characterization of structure and chemistry. This composition is a canonical ESO which has been shown to be entropy-stabilized by Rost et al.[18] We hypothesized that cations such as Cu or Zn segregate to GBs in the polycrystalline single-phase (Co,Cu,Mg,Ni,Zn)O ESO. This facilitates the formation of (previously reported) secondary phases, which may form at GBs and/or in grain interiors. These secondary phases affect the ESO's electrical transport mechanism(s) through the altered point defect chemistry of grain interiors and GBs. Finally, we hypothesized that the structure and composition of HIs in ESOs is relevant to secondary phase morphology and overall charge transport, and should be considered when designing/fabricating electronic devices such as thin films with optimized HI properties.[29]

To test our hypothesis, we used heat treatment to control the formation of a multiphase microstructure comprising ESO grains with inter/intragranular secondary phase particles. We quantified the structure and composition of single-phase and multiphase ESOs, and their GBs and HIs using atomic-resolution scanning transmission electron microscopy (STEM) imaging and (sub-)nanoscale spectroscopy by energy dispersive X-ray spectroscopy (EDS) and electron energy-loss spectroscopy (EELS). While GBs have been recently studied in CCOs,[30,31] to our knowledge this is the first report of sub-nanometer chemical composition and atomic structure of ESO GBs and HIs, which is necessary as these planar defects are inevitable in the large-scale production of ceramic oxides.[27,32] Experimental observations of GB segregation were interpreted with the assistance of density functional theory (DFT) calculations, though the complexity of the GBs observed precluded a general fundamental understanding of atomistic segregation mechanisms. Importantly, secondary phase formation influences defect chemistry, which introduces new charge carriers and changes the electrical transport measured here by electrochemical impedance spectroscopy (EIS). Detailed exploration of GBs and HIs revealed that GBs are key in the microstructure formation and conductivity mechanisms while HIs define secondary particle shape within ESO grain interiors. These findings deepen our basic understanding of structure-function-processing relationships in an emerging class of highly promising materials which will guide the design and engineering of ESO compositions with tunable microstructure, electrical conductivity, and composite-derived multifunctionalities for a broad range of applications.

2. Results and Discussion

2.1. Homogeneous Bulk Composition and Copper Segregation to the Grain Boundaries in Single-phase ESO

It is well known that GBs can play a governing role in a ceramic's overall electrical properties.[27,32–36] To shed light on the conduction mechanisms in single-phase (Co,Cu,Mg,Ni,Zn)O (called ESO-single), atomic/nano scale structure and chemical composition of grain interior and GBs were investigated. We first confirmed the homogeneity of all cations and O^{2-} in grain interior using XRD, scanning electron microscopy (SEM), and STEM-EDS (**Figure 1**a–c; Figure S1, Supporting Information). Next, segregation of Cu and a Si- and Ca-rich amorphous phase to the GB was detected, which is a common result of ceramic fabrication. A representative elemental distribution profile across a GB demonstrates two ≈1 nm thick layers of Cu segregated to the two sides of the GB planes, while the amorphous phase segregates to the GB core (Figure 1d; Figure S2, Supporting Information). CuO is not stable in the rocksalt structure due to a degeneracy in the electronic configuration and prefers to crystallize into a tenorite crystal structure. This degeneracy leads to a Jahn–Teller effect and a distortion in the (Co,Cu,Mg,Ni,Zn)O crystal structure,[37,38] causing some Cu ions to segregate from grain interiors to GBs to minimize the free energy, allowing the entropy stabilization of a single-phase rocksalt ESO. Our DFT results support this claim by showing that GB energy decreases as the Cu ions in the crystal interior preferred to occupy the distorted GB sites in a single-phase rocksalt ESO, Figure S3 (Supporting Information). While this is not an exact simulation of the experimentally observed interface (the complex structure of an amorphous Si-rich film cannot be captured with DFT), it demonstrates that Cu ions prefer to occupy crystallographically disordered defect sites which is consistent with the observation of Cu ions adjacent to the GB in the TEM measurements. The amorphous phase at the GB is made of raw material impurities, which is typically observed to block ion transport in polycrystalline ceramics.[39] However, as discussed below, importantly we do not observe any impedance response attributable to these intergranular phases, and thus we assume the GBs in ESO-single do not contribute an impedance response to the sample's overall response.

2.2. Formation of Intragranular and Intergranular Secondary Phase Particles in Heat Treated ESOs

2.2.1. Chemical Composition, Structure and Morphology of Secondary Phase Particles

ESOs undergo a reversible phase transformation during heat treatment, forming Cu-rich and Co-rich oxide particles.[26] The

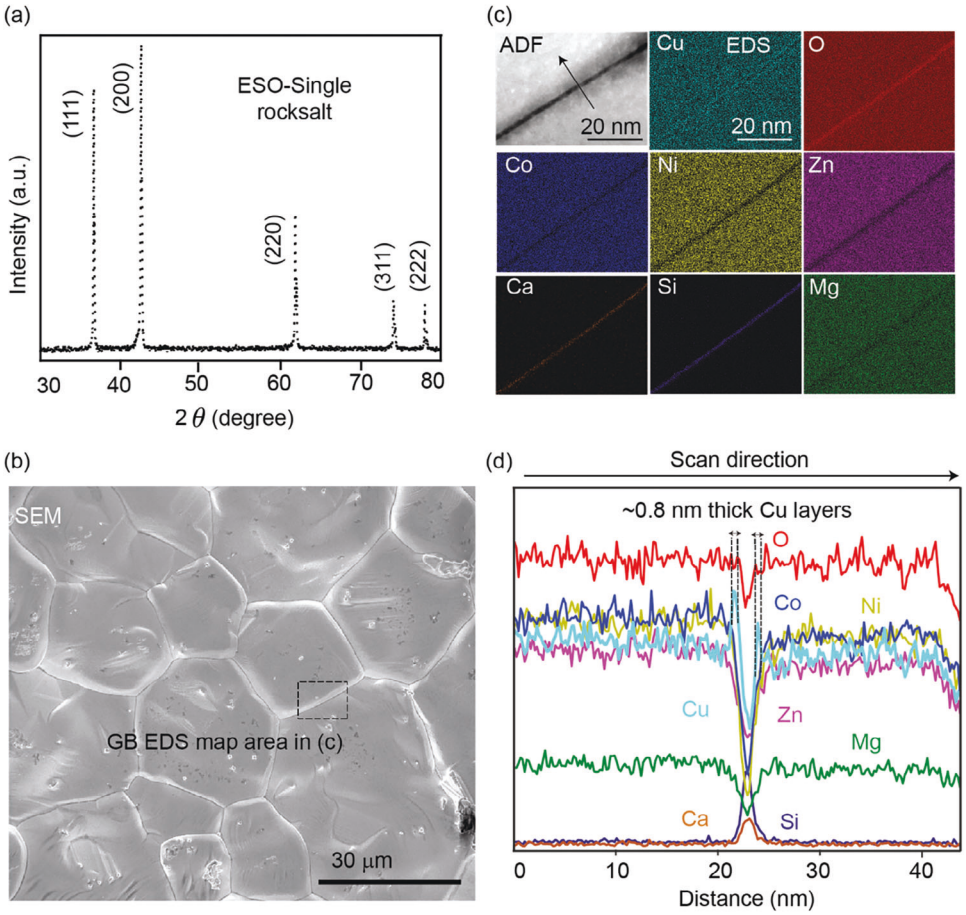

Figure 1. Segregation of Cu to GBs in single-phase ESO. a) XRD shows that ESO-single has a rocksalt crystal structure: Fm $\bar{3}$ m (225) ICSD–52026. b) SEM image of ESO-single. c) STEM-EDS chemical mapping of a GB in b, demonstrating Cu and Si-rich GB phase. d) Elemental distribution across the GB map in c, in the direction of the black arrow.

heat treatment temperature used to form the multiphase state (700 °C) is low enough that the Gibbs free energy of the single-phase state is insufficient to overcome the Gibbs free energy of the multiphase state. We therefore propose that our multiphase samples are enthalpy- stabilized, while our single-phase sample is entropy-stabilized. To understand the effect of heat treatments on the atomic/nanoscale composition, structure, and morphological features of the secondary phases, 2 and 24 h heat treated ESO pellets (called ESO-2h and ESO-24h, respectively) were explored using XRD, STEM imaging, EDS, EELS in **Figure 2**. For ESO-2h, XRD shows secondary phase peaks related to tenorite and spinel structures (Figure 2a). Using STEM-EDS, we observed the formation of nanoscale intergranular Cu-rich oxide particles at some GB sites, as well as the homogeneous distribution of all elements in the grain interiors, Figure 2b. The Cu-rich particles mainly consist of Cu and O, with some Mg and Zn, quantified using STEM-EELS (Section 2.2.2.). Cu segregation was still observed at the GBs not covered with secondary phases suggesting that as the ESO is annealed, Cu segregates to the GBs, facilitating the formation of the entropy-stabilized single-phase ESO. The formation of Cu-rich secondary phases is also expected to produce adjacent Cu depletion zones in the grains.[25,40]

The XRD results from ESO-24h show a larger number of secondary phase peaks with higher intensities (with respect to ESO rocksalt primary peaks) related to tenorite and spinel structures (Figure 2c). Additionally, intragranular Cu-rich and Co-rich oxide particles form in the grain interiors, Figure 2d. It is hypothesized that after Cu layer formation, Cu-rich secondary phase particles cover all the GBs, creating Cu depletion zones in the grains directly adjacent to particle-covered GBs.[25,40] Cu-rich secondary phase particles continue to nucleate and grow throughout grain interiors, where Cu has not been depleted. For the Co-rich particles, it is hypothesized that Co can fill the Cu vacancies (V''_{Cu}) created during the formation of Cu-rich particles, which increases local Co concentration and enables the nucleation of Co-rich particles. As discussed below, Cu-rich and Co-rich oxide particles grow into anisotropic needle-like and equiaxed morphologies, respectively.

The crystal structure of phases was determined by atomic-resolution HAADF imaging performed at a triple junction of ESO grain interior/Cu-rich oxide phase/Co-rich oxide phase in ESO-24h, **Figure 3**a. FFT patterns calculated from the HAADF image confirm that Cu-rich and Co-rich secondary phases have tenorite and spinel crystal structures, Figure 3b–d.

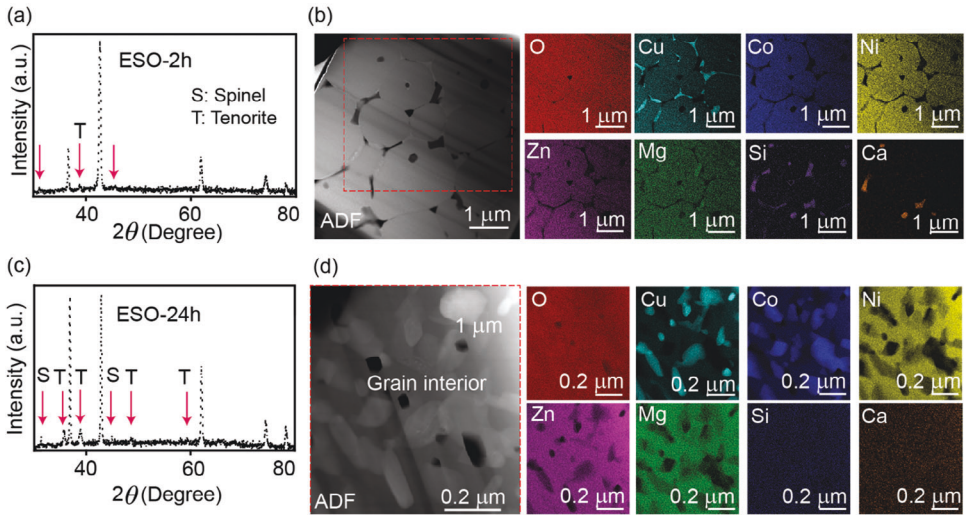

Figure 2. Formation of Cu-rich and Co-rich oxide secondary particles in multiphase ESOs. a) XRD of ESO-2h showing peaks of secondary phases (CuO tenorite: Fm $\bar{3}$ m (225) ICSD–52026 and Co_3O_4 Spinel: Fd $\bar{3}$ mS (227) ICSD–36256). b) ADF-STEM and EDS chemical maps of grains indicating the homogenous distribution of cations and oxygen and intergranular Cu-rich tenorite particles in ESO-2h. c) XRD of ESO-24h showing more visible peaks of secondary phases. d) ADF-STEM and EDS chemical maps of a grain interior showing Cu-rich and Co-rich secondary phase particles inside grains after 24 h of heat treatment at 700 °C.

2.2.2. Structure and Chemical Composition of Heterointerfaces and Their role in Secondary Phase Particle Morphology

To reveal the role of HIs in phase transformation and conductivity, the atomic structure and chemical composition of the ESO-24h HIs were investigated. We observed that Cu-rich tenorite phase often adopts a needle-like morphology, with straight sides and curved tips (**Figure** 4a). Given the differences in the crystal structure and atomic arrangements of Cu-rich tenorite and grain interior ESO rocksalt (cubic), misfit strain is expected at both HIs. Atomic-resolution HAADF-STEM images confirmed that needle tips were semi-coherent and curved, with a lattice mismatch of ≈5% (Figure 4c). This value agrees with the misfit values reported for semi-coherent HIs in metals[41] and ceramics.[42] The higher lattice mismatch at needle tips compared to the sides is compensated for by the formation of edge dislocations. Edge dislocations allow for faster cation diffusion across needle tips compared to the sides, elongating the needle-like morphology as the secondary phases grow. Two sets of edge dislocations were detected at this HI using MAADF- and BF-STEM imaging. The first dislocation set with the Burgers vector, $\overrightarrow{b1}$, is parallel to the HI with a dislocation spacing of 5 nm. The second dislocation with the Burgers vector, $\overrightarrow{b2}$, is perpendicular to the HI with a dislocation spacing of 4 nm. The existence of two non-parallel sets of dislocations partly relieves the interfacial coherency strain, while maintaining the residual long-range strain.[43] The incoherent (distorted) areas are the dark regions visible in the BF-STEM micrograph.

Unlike Cu-rich tenorite needles, Co-rich spinel particles form equiaxed morphologies with one HI type (Figure 4b), which is a coherent HI with some lattice misfit strain. Even though the Co-rich spinel and ESO rocksalt phases are both cubic, differences in lattice parameters and atomic arrangements cause a misfit strain of ≈1%. Therefore, variations in contrast observed at this HI in MAADF and BF-STEM modes (diffraction and strain contrast), suggest the existence of misfit-induced elastic strain (Figure 4d).

No segregation or depletion of cations is detected at either HI using STEM-EELS, suggesting a smooth transition from one phase to the other at the needle tip (Figure 4e), spinel/ESO HI (Figure 4f), and needle side (Figure S4, Supporting Information). Therefore, we conclude that the contrast variations are solely related to lattice distortion. All HIs observed in this study have wider (≈3–5.5 nm) compositional widths—the distance over which there is a composition gradient (Figure 4e,f; Figure S4, Supporting Information), than structural widths (1–2 nm)—the distance over which there is lattice distortion caused by the interface (Figure 4c,d). The considerably larger compositional width is a known characteristic of diffuse HIs seen in phase transformed CCMs such as precipitate-hardened high-temperature alloys.[44,45] The wider compositional widths at the ESO HIs are attributed to the longer-range diffusion of ions in ESOs due to the distorted nature of the crystal structure at the atomic level.[46]

Using STEM-EELS, the stoichiometry of the Cu-rich tenorite phase at the needle tip was measured to be $Cu_{0.73}Mg_{0.08}Zn_{0.19}O$, which we speculate forms by simultaneous co-segregation of Cu, Mg, and Zn. The stoichiometry measured at the needle side was $Cu_{0.53}Mg_{0.2}Zn_{0.27}O$, suggesting slight changes in Mg and Zn dissolution in CuO leading to a composition gradient across the needle-like particle, which we attribute to the interaction between strain, cation solubility, and diffusivity across the HI;[45,47–49] while this has not been elucidated in the literature, it could provide additional degrees of secondary phase tunability. Negligible signals detected from Co and Ni suggest their absence in the tenorite phase. The stoichiometry of the Co-rich spinel phase was measured to be $Co_{2.54}Cu_{0.02}Ni_{0.06}Zn_{0.38}O_4$. For quantified stoichiometries of secondary phase particles, see Table S1 (Supporting Information).

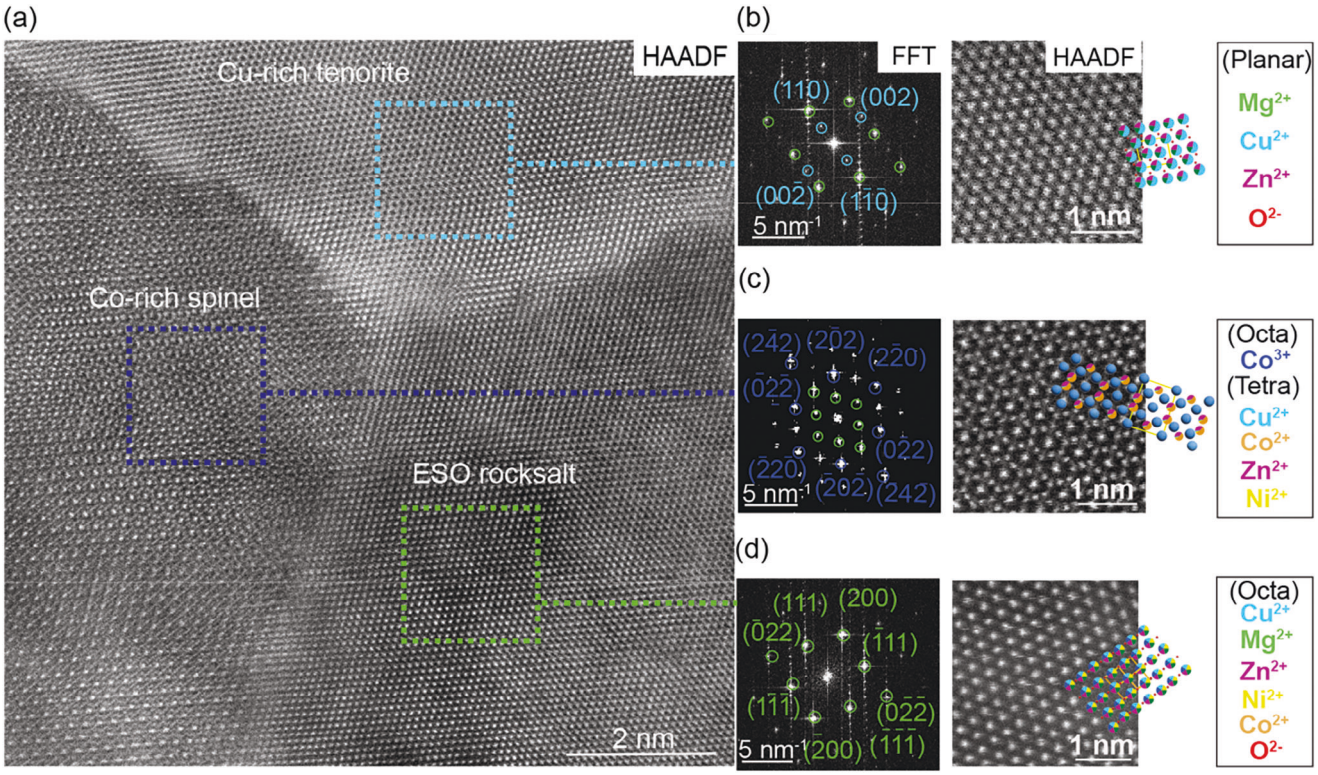

Figure 3. Atomic structure of a triple junction in ESO-24h. a) HAADF-STEM image of ESO grain interior/Cu-rich tenorite/Co-rich spinel triple junction. b–d) Indexed FFT patterns, atomic-resolution HAADF micrographs, and atomic model overlays of (b) Cu-rich tenorite, (c) Co-rich spinel, and (d) ESO rocksalt grain interior.

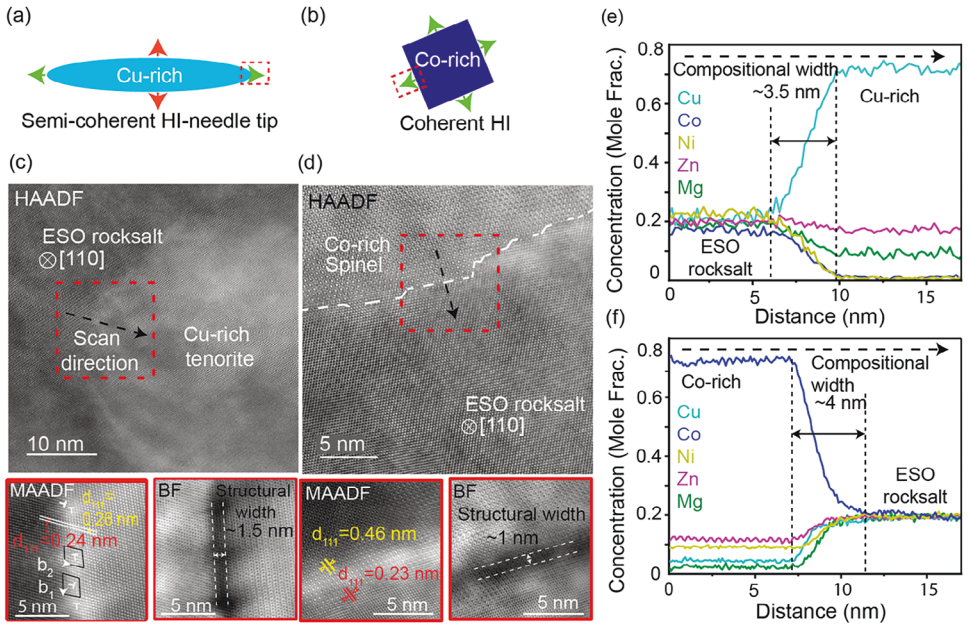

Figure 4. Coherent and semi-coherent HIs with no elemental segregation or depletion in ESO-24h. Atomic structure and composition of two HIs and their correlation to secondary phase particle morphology. a) The needle-like morphology of a Cu-rich tenorite particle. b) The equiaxed morphology of a Co-rich spinel particle. c) HAADF/BF-STEM images of a tenorite/ESO HI at a needle tip, with expanded views of the red dashed zone. d) HAADF-STEM image of a spinel/ESO HI with expanded views of the red dashed zone in MAADF and BF modes. e) STEM-EELS cation composition profile across the tenorite/ESO HI at needle tip f) STEM-EELS cation composition profile across the spinel/ESO HI.

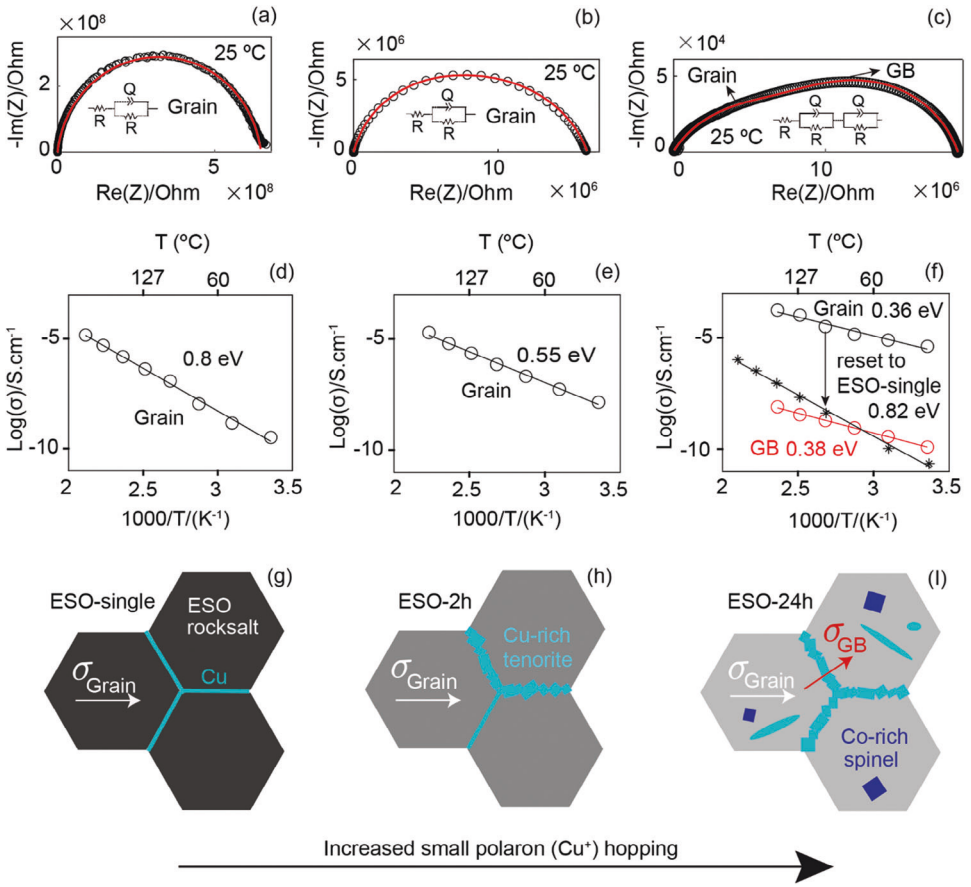

Figure 5. Electrical conductivity of single and multiphase ESOs with respect to the atomic/nano-scale structure and composition. Representative Nyquist plots collected from a) ESO-single, b) ESO-2h and c) ESO-24h at 25 °C. Log_{10}(conductivity) as a function of temperature for all three pellets, with Ag electrode for d) ESO-single and e) ESO-2h and f) ESO-24h. Proposed conductivity pathways in g) ESO-single, h) ESO-2h and i) ESO-24h.

2.3. Changes in Electrical Conductivity and Activation Energy with Heat-Treatment-Induced Phase Transformations

To investigate the relationship between microstructure and conduction mechanism, the electrical conductivities of ESO-single, ESO-2h, and ESO-24h pellets were determined using AC impedance spectroscopy and equivalent circuit model fitting. Porous O^{2-} permeable fired Ag paste was used as electrodes. The Nyquist plots of ESO-single only exhibit one "RQ" arc, attributed to the total impedance response of the pellet (grains and GBs), **Figure** 5a, Figures S5–S7 (Supporting Information). This suggests that the GBs (Figure 1) do not form a space charge layer that would show up as a second distinct arc. Based on the slope of the conductivity as a function of inverse temperature (Figure 5d), an activation energy of 0.80 eV is calculated for charge transport in the distorted rocksalt grain interiors from Arrhenius plots of conductivity (Figure S8, Supporting Information).

We attribute conductivity in this sample to electronic hopping between reduced Cu polarons, Cu'_{Cu} which are known from DFT to accommodate oxygen sub-stoichiometry.[50] Compositional complexity in ESOs is known to facilitate the formation of localized charges. For example, Cu^+ is known to exist in this rocksalt ESO given the relatively weak Cu—O bonds, according to DFT, X-ray photoelectron spectroscopy (XPS), and anion sublattice distortion measurements.[46,50,51] Moreover, the starting binary oxides are strongly insulating (MgO)[52] or p-type (CuO,[53,54] CoO,[55] NiO[56,57]) and n-type (ZnO)[58] semiconductors within the 25–200 °C temperature range used for conductivity measurements in this work (**Table 1**), supporting our assumption that transport is electronic. As shown below, the 0.8 eV conductivity activation energy for Cu^+/Cu^{2+} polaron hopping in ESO-single is relatively high compared to ESO-2h and ESO-24h samples (Figure 5e,f), which we believe stems from the relatively low Cu^+ polaron concentration and concomitant relatively large polaron separation distance, as well as defect association effects between Cu^+ and oxygen vacancies that increase the polaron migration barrier.[59] To assess the possible impact of entropy stabilization on electronic conductivity, the ESO's electronic conductivity is compared to that of the starting binary oxides, Table 1. ESO-single's conductivity is within the range of values for the binary oxides, suggesting that entropy stabilization does not play a decisive role in governing the electronic conductivity of this ESO.

Like ESO-single, the ESO-2h Nyquist plots were best fit to an R-RQ circuit model (Figure 5b; Figure S9–S11, Supporting Information) attributed to the rocksalt grain interior contribution. A conductivity activation energy of 0.55 eV is calculated for ESO-2h (Figure 5e; Figure S8, Supporting Information), which is consistent with that of Cu^+/Cu^{2+} small polaron hopping reported

Table 1. Electrical conductivity and conductivity activation energy values measured for ESO-single in this work and small polaron hopping in binary transition metal oxides from literature.

Oxide (carrier)	Conductivity [S cm^{-1}]	Activation energy [eV]	Temperature [°C]	References
ESO (Cu^{+}/Cu^{2+} n-type small polaron)	3×10^{-10}	0.8	25	This work
CuO (p-type semi.)	4×10^{-2}	0.21, 0.31 0.27 across GB	30	[53,54]
CoO (p-type semi.)	6.3×10^{-10}	0.68	25 (extrapolated)	[55]
NiO (p-type semi.)	10^{-5}	0.46	25 (extrapolated)	[56,57]
ZnO (n-type semi.)	5×10^{-9}		1100	[58]
MgO	10^{-15}	2.8	227	[52]

previously in this ESO (Table S2, Supporting Information).[24,60,61] In ESO-2h, the formation of Cu-rich tenorite particles at GBs requires the formation of copper vacancies, V''_{Cu}, in the grains that are charge compensated by oxygen vacancies, $V^{\bullet\bullet}_{O}$, which are known (from DFT[50]) to form preferentially as nearest neighbors to Cu^{+}. Increasing the $V^{\bullet\bullet}_{O}$ concentration in the ESO grains thus increases the concentration of Cu^{+} and lowers the small polaron site separation distance, leading to a measured electronic conductivity enhancement of ≈2 orders of magnitude at 25 °C.

For ESO-24h, the two overlapping arcs detected at higher and lower frequencies are fit to a series R-RQ-RQ circuit, with each RQ corresponding to grain interior or GBs, respectively (Figure 5c; Figures S12–S14, Supporting Information). The measured grain interior conductivity activation energy is 0.36 eV (Figure 5f; Figure S8, Supporting Information), attributed to Cu^{+} small polaron hopping caused by further increased $V^{\bullet\bullet}_{O}$ concentration as in the ESO-2h. This is due to further depletion of Cu and Co upon secondary phase formation. Assuming the intensity of main XRD peak is proportional to the volume fraction of each phase, the formation of Cu-rich tenorite particles at GBs and Cu-rich tenorite and Co-rich spinel particles in grain interiors may increase the concentration of Cu site vacancies by up to 6%, and the Co site vacancies by up to 2% relative to the pristine ESO rocksalt (Figure S15, Supporting Information). We believe the Cu-rich and Co-rich particles do not contribute to the grain interior conductivity because they are isolated within the grains and facilitate charge carriers of the opposite charge (p-type in CuO and CoO vs n-type in ESO[53,55]). Therefore, we conclude that the enhanced ESO-24h grain interior electronic conductivity of ≈4 orders of magnitude compared to ESO-single is due to changes in grain interior defect chemistry caused by additional Cu-rich tenorite formation at GBs, as well as Cu-rich tenorite and Co-rich spinel secondary phase particles in grains.[8]

For the GB conductivity, we observe a single thermally-activated conduction mechanism at 25–150 °C with an activation energy of 0.38 eV, attributed to the local electron hopping across the GBs containing Cu-rich tenorite particles. The specific GB conductivity values are ≈4 orders of magnitude lower than that of the grain interior, suggesting very poor electron conduction through CuO tenorite particles at the GB. Schematics in Figure 5g–i show the correlation between microstructure and electrical conductivity as a function of heat-treatment-induced phase transformations in ESO-single, 2h, and 24h. The total conductivity values measured for ESO-24h (grain interior plus GBs) increased compared to that measured for ESO-single and ESO-2h, demonstrating enhanced electrical conduction in this ESO caused by heat-treatment-induced phase transformations. Additional heat treatment of ESO-24h at 850 °C returns the electronic conductivity and conductivity activation energy to the single-phase value (Figure 5f- plotted with star icons). This highlights the exciting prospect of designing resistive switching devices by balancing enthalpy-stabilized secondary phase formation with entropy-stabilized second phase annihilation.

3. Conclusions

The origin of reversible enhancements in electronic conduction in a single-phase ESO and two multiphase ESOs (heat treated at 700 °C for 2 and 24 h) were detailed with respect to secondary phase content, atomic/nano-scale structure and composition, and defect chemistry. We found that the single-phase ESO has two Cu layers at the surfaces of the ESO crystals forming GBs, stabilizing a single-phase ESO rocksalt solid solution with homogeneous distribution of all elements in the grain interiors. EIS conductivity activation energy measurements suggest that ESO-single is conducting Cu^{+} small polarons by hopping through the rocksalt structure. It is observed that the GBs do not have a specific impact on electronic conduction in this sample. By comparing ESO-single's electronic conductivity to that of the constituent binary oxides, entropy stabilization seems to have little governing effect on electronic transport in this ESO. Upon 2 h of heat treatment, Cu^{2+} leaves the ESO, forming intergranular Cu-rich tenorite particles covering some but not all the GBs. The added V''_{Cu} are compensated by the formation of $V^{\bullet\bullet}_{O}$, facilitating reduction of Cu^{2+} to Cu^{+} in the grains, and enhancing electronic conduction up to ≈2 orders of magnitude with a decreased activation energy to 0.55 eV. After 24 h of heat treatment, Cu-rich tenorite phase is assumed to cover all GBs, followed by the nucleation and growth of intragranular Cu-rich tenorite and Co-rich spinel particles in the grain interiors. While Cu-rich tenorite particles at the GBs slow cross-GB electron conduction, Cu^{+} small polaron conduction is shown to further enhance conductivity of grain interiors by 2–3 additional orders of magnitude, due to the

extensive formation of $V_{Cu}^{//}$ and $V_{Co}^{//}$ which are charge compensated by $V_O^{\bullet\bullet}$. The overall total conductivity in ESO-24h is higher compared to ESO-single and ESO-2h which is attributed to heat-treatment-induced phase transformations. The impact of high entropy and entropy stabilization on electronic transport in this material appears to be an indirect one, in that the ESO offers tunable defect chemistry (through heat-treatment-induced secondary phase formation) which subsequently enhances conductivity. Importantly, the reversibility of the conductivity enhancement points towards the possibility of designing resistive switching materials by balancing entropy-stabilized single-phases with enthalpy-stabilized composites.

Probing the cation composition profiles across the HIs formed between ESO and secondary phases (in ESO-24h) revealed diffuse interfaces with a relatively large transitional compositional width. On the other hand, atomic structures observed suggest the formation of coherent and semi-coherent HIs with misfit strain. Unlike the equiaxed Co-rich spinel particles, intragranular Cu-rich tenorite particles form in anisotropic needle-like morphologies due to the existence of misfit dislocation at needle tips, allowing faster diffusion and growth in this direction. Our findings suggest the negligible (if any) role of HIs in the conduction mechanisms of the ESO. This work demonstrates the ability to reversibly tune the electrical transport mechanism of ESOs via multiphase design, providing additional degrees of freedom to engineer a wider range of microstructures and compositions which will lead to novel complex concentrated materials.

4. Experimental Section

Synthesis and Sintering: (Co,Cu,Mg,Ni,Zn)O ESO nanopowders were synthesized via solid-state methods using CoO (50 nm particle size, 99.7 wt% purity), CuO (25–55 nm, 99.95%), MgO (50 nm, 99.95%), NiO (18 nm, 99.98%), and ZnO (18 nm, 99.95%) from US Research Nanomaterials Inc (Houston, TX, USA). Starting constituent oxides were blended in equimolar amounts using a mortar and pestle, followed by planetary ball milling (Fritsch GmbH, Idar-Oberstein, Germany) for 3 h using a silicon nitride jar and milling media with the powder suspended in isopropanol. Conventional and spark plasma sintering (SPS) were used to consolidate the blended oxide nanopowders into fully dense, bulk pellets with varying grain sizes. Conventional sintering was done inside an elevator furnace using 1100 °C for 12 h (CM Furnaces, Bloomfield, NJ, USA). SPS was done using a Fuji model 825 SPS at 900 °C under a pressure of 100 MPa for 2 h. Microstructure and crystal structure of pellets were studied using XRD (Ultima III, Rigaku, Tokyo, Japan) and scanning electron microscopy (SEM) (Magellan 400, Thermo Fisher Scientific, Waltham, Massachusetts).

Heat Treatment: Based on the previous work,[8] this ESO formed a single-phase structure when heat treated and quenched from temperatures above 850 °C. If the single-phase ESO was then heat treated and quenched from the temperature range of 650–850 °C, a multiphase ESO formed. It was observed that heat treatments at 700 °C exhibit higher secondary phase content formation, yielding a maximum of ≈17 at. % Cu-rich phase and ≈11 at. % Co-rich phase.[26] In this study, one pellet was kept in the as-sintered single-phase form and two other pellets were heat treated for 2 and 24 h at 700 °C to produce multiphase ESOs with varying secondary phase content. The pellets are labeled as ESO-single, ESO-2h and ESO-24h.

Electrochemical Impedance Spectroscopy: AC electrochemical impedance spectroscopy (EIS) was used to measure the electrical conductivity and activation energies for ESO-single, ESO-2-h, and ESO-24-h. Conductivity was measured at temperatures 25–200 °C to avoid inducing phase transformations (which occur at higher temperatures) during EIS. O^{2-} non-blocking porous electrodes were fabricated using Ag paste (Fuel Cell Materials, Columbus, OH) that was applied on the polished surfaces of all pellets and annealed at 400 °C for 1 h. EIS was performed in air using a BioLogic SP-200 potentiostat (BioLogic Sciences Instruments, Seyssinet-Pariset, France). An excitation voltage of 50–150 mV over the frequency range of 1 mHz–7 MHz was used. Pellets were heated from 25–200 °C (in 50 °C increments) inside a HFS600E-PB4 probe stage with a T96 system controller (Linkam Scientific Instruments, Redhill, United Kingdom).

Impedance data were collected at each dwelling temperature after the impedance response became stable over time. Nyquist plots were fit to equivalent circuit models containing one or two parallel resistor-constant phase element (RQ) subcircuits (Z-fit mode in BioLogic's EC-Lab). Here, *Q* represents the constant phase element, with each RQ subcircuit corresponding to a specific electrochemical response. The Nyquist plots from ESO-single and ESO-2h were fit to a single RQ circuit model, representing pellet total resistance. The Nyquist plots from ESO-24h were fit to a 2RQ circuit model, representing two different resistance contributions in the form of two overlapping arcs. Equation (1) was used to calculate the total and grain interior conductivity:

$$\sigma = \frac{L}{AR} \tag{1}$$

where *L* and *A* are pellet thickness and cross-section area, respectively. For total conductivity, *R* is total pellet resistance (i.e., the diameter of the grain interior/bulk arc plus grain boundary arc in Nyquist plots). For grain conductivity, *R* is the diameter of just the grain interior/bulk arc. The specific GB conductivity for ESO-24h was calculated using Equation (2):

$$\sigma_{GB} = \frac{L}{AR}\left(\frac{g}{G}\right) \tag{2}$$

where *g* and *G* are GB thickness and pellet average grain size, respectively. Conductivity activation energies were calculated using the slopes of the Arrhenius conductivity plots with Equation (3):

$$\sigma = \frac{\sigma_0}{T}\exp\left(\frac{-E_a}{k\,T}\right) \tag{3}$$

where σ is conductivity, σ_0 is the conductivity pre-exponential factor, E_a is the activation energy of charge transport, *k* is the Boltzmann constant, and *T* is absolute temperature.

STEM Sample Preparation: Aberration-corrected STEM was used to characterize the structure and composition of grain interiors and selected GBs in ESO-single, as well as atomic structure, composition, and morphology of the secondary phases formed during heat treatments in ESO-2h and ESO-24h. TEM samples of ESO-single, ESO-2h, and ESO-24h were prepared by focused ion beam (FIB) lift-out in a dual-beam SEM/FIB (Tescan, Kohoutovice, Czech Republic) equipped with Ga^+ focused beam.[62] To protect the TEM sample from ion-beam damage, a 2 µm thick platinum layer was deposited on each surface.

STEM Energy-Dispersive X-ray Spectroscopy and Electron Energy-Loss Spectroscopy: Atomic-resolution scanning transmission electron microscopy (STEM) in high-angle annular dark-field (HAADF), medium-angle annular dark-field (MAADF), and bright-field (BF) modes, as well as energy-dispersive X-ray spectroscopy (EDS), and electron energy-loss spectroscopy (EELS) were performed using a JEOL Grand ARM300CF (200–300 KeV, JEOL Tokyo, Japan). Fast Fourier Transform (FFT) patterns calculated from atomic-resolution images were used to identify the crystal structures. Microscope data were processed using Gatan Digital Micrograph (Gatan, Pleasanton, CA). EELS and EDS backgrounds were subtracted using the Hartree–Slater cross-section and Kramers background correction mode in Digital Micrograph, respectively. The following peaks were used for the analysis: O Kα (0.525 keV), Mg Kα (1.254 keV), Ni Kα (7.480 keV), Co Kα (6.931 keV), and Kβ (7.649 keV), Cu Kα (8.046 keV) and Kβ (8.904 keV), and Zn Kα (8.637 keV) and Kβ (9.570 keV). STEM-EDS was used to identify the chemical composition of bulk and GBs in

ESO-single, as well as secondary phase particles and GBs in ESO-2h and ESO-24h. STEM-EELS was used to quantify the stoichiometry of secondary phase particles and the distribution of cations across HIs.

Density Functional Theory Calculations: First-principles calculations were performed within the DFT framework using the Vienna ab initio simulation package (VASP)[63,64] within the generalized gradient approximation (GGA) using the Perdew–Burke–Ernzerhof for solids (PBEsol) exchange–correlation functional.[65] Projector augmented wave (PAW) pseudopotentials with a plane–wave cutoff energy of 600 eV were used for all the calculations. The magnetism of Co, Cu, and Ni was treated with the PBEsol collinear spin density approximation in the GGA with a Hubbard U (GGA + U) scheme.[66–68] The Coulomb parameter (U) was applied for these elements to account for the increased Coulomb repulsion between the semi-filled 3d states. U = 6 was used, as this value can obtain the correct ground state phases for the oxides of transition metals considered here. Spin-polarized calculations were performed where the magnetic moments of Co, Cu, and Ni in the rocksalt phase were initiated in the antiferromagnetic II type state. The equilibrium bulk ESO rocksalt structure was determined using the Monkhorst-pack k-point mesh[69] with convergence energy of 10^{-5} eV atom^{-1} and convergence atomic force of 0.01 eV Å^{-1}. The computed lattice parameter of bulk ESO rocksalt is 4.23 Å, which matches very well with our experimentally observed value of 4.1–4.2 Å.

To understand the experimentally observed clustering of Cu at GBs in rocksalt (Co,Cu,Mg,Ni,Zn)O ESO, a Σ5 (310) GB was examined in the ESO rocksalt. This interface was chosen as a model boundary because it has multiple different potential segregation sites and has been commonly examined to understand different GB properties in a variety of metals[46–48,51,70,71] and metal oxides[72–74] due to its high symmetry and low energy structure. The simulation cell had dimensions of $41.78 \times 4.26 \times 6.85$ Å^3 and contained 120 atoms including 60 metal atoms in equiatomic concentration and 60 oxygen atoms. The atoms were relaxed at their positions using a gamma-pack k-point mesh to an energy convergence of $<10^{-5}$ eV while maintaining a constant volume and shape of the GB sample. The GB energy (E_{gb}) was calculated as the difference between the energy of the GB simulation cell (E) and the energy of equilibrium ESO rocksalt (E_{bulk}) with the same number of atoms per unit area of the GB plane (S) using Equation (4):

$$E_{gb} = \frac{E - E_{bulk}}{2S} \tag{4}$$

To examine the clustering of Cu ions at the GB, different GB samples were prepared with 16.66, 33.33 and 50 at. % Cu-ions in the GB region while maintaining an equiatomic concentration of metal ions in the overall simulation cell. GB concentration was calculated as the number of Cu-ions divided by the total number of metal ions in the GB region. Each of the samples was energetically relaxed to obtain an equilibrium structure, followed by GB energy calculation using Equation (4).

Supporting Information

Supporting Information is available from the Wiley Online Library or from the author.

Acknowledgements

The authors thank S. M. Haile (Northwestern University) and H. L. Tuller (Massachusetts Institute of Technology) for valuable comments. This research was primarily supported by the National Science Foundation Materials Research Science and Engineering Center program through the UC Irvine Center for Complex and Active Materials (DMR-2011967). WJB and HV acknowledge partial support from the UCI new faculty startup funding. The authors acknowledge the use of facilities and instrumentation at the UC Irvine Materials Research Institute (IMRI) supported in part by the National Science Foundation Materials Research Science and Engineering Center program through the UC Irvine Center for Complex and Active Materials (DMR-2011967).

Conflict of Interest

The authors declare no conflict of interest.

Author Contributions

H.V. and W.J.B. devised the study. H.V. wrote the manuscript and provided the EIS conductivity measurement, STEM characterization data and analysis. B.X.L. contributed to the analysis and interpretation of EIS data. J.C., A.D.D., and J.M.S. provided the pellets, XRD and SEM. P.G. and T.J.R. performed the DFT simulations and associated calculations. H.V. and W.J.B. developed the theory and the discussions. All authors reviewed and revised the final manuscript. W.J.B. supervised the study.

Data Availability Statement

The data that support the findings of this study are available from the corresponding author upon reasonable request.

Keywords

electrical conductivity, entropy-stabilized oxides, grain boundaries, interfaces, polarons, scanning transmission electron microscopy

Received: December 12, 2023
Published online:

[1] Y. Zeng, B. Ouyang, J. Liu, Y.-W. Byeon, Z. Cai, L. J. Miara, Y. Wang, G. Ceder, *Science* **2022**, *378*, 1320.
[2] D. Bérardan, S. Franger, D. Dragoe, A. K. Meena, N. Dragoe, *Phys. Status Solidi RRL – Rapid Res. Lett.* **2016**, *10*, 328.
[3] C. M. Rost, D. L. Schmuckler, C. Bumgardner, M. S. Bin Hoque, D. R. Diercks, J. T. Gaskins, J.-P. Maria, G. L. Brennecka, X. Li, P. E. Hopkins, *APL Mater.* **2022**, *10*, 121108.
[4] D. Wang, S. Jiang, C. Duan, J. Mao, Y. Dong, K. Dong, Z. Wang, S. Luo, Y. Liu, X. Qi, *J. Alloys Compd.* **2020**, *844*, 156158.
[5] B. Zhao, Z. Yan, Y. Du, L. Rao, G. Chen, Y. Wu, L. Yang, J. Zhang, L. Wu, D. W. Zhang, R. Che, *Adv. Mater.* **2023**, *35*, 2210243.
[6] K. Wang, W. Hua, X. Huang, D. Stenzel, J. Wang, Z. Ding, Y. Cui, Q. Wang, H. Ehrenberg, B. Breitung, C. Kübel, X. Mu, *Nat. Commun.* **2023**, *14*, 1487.
[7] L. Su, H. Huyan, A. Sarkar, W. Gao, X. Yan, C. Addiego, R. Kruk, H. Hahn, X. Pan, *Nat. Commun.* **2022**, *13*, 2358.
[8] A. D. Dupuy, X. Wang, J. M. Schoenung, *Mater. Res. Lett.* **2019**, *7*, 60.
[9] H. Guo, X. Wang, A. D. Dupuy, J. M. Schoenung, W. J. Bowman, *J. Mater. Res.* **2022**, *37*, 124.
[10] H. Guo, C. Mead, M. H. Balingit, S. Shah, X. Wang, M. Xu, I. Tran, T. Aoki, J. D. Samaniego, K. L. Gilliard-AbdulAziz, L. J. Lauhon, W. J. Bowman, *Matter* **2023**, *7*, 1.
[11] A. Sarkar, Q. Wang, A. Schiele, M. R. Chellali, S. S. Bhattacharya, D. Wang, T. Brezesinski, H. Hahn, L. Velasco, B. Breitung, *Adv. Mater.* **2019**, *31*, 1806236.
[12] Y. Ning, Y. Pu, Q. Zhang, S. Zhou, C. Wu, L. Zhang, Y. Shi, Z. Sun, *Ceram. Int.* **2023**, *49*, 12214.
[13] J. Xiao, X. Li, K. Tang, D. Wang, M. Long, H. Gao, W. Chen, C. Liu, H. Liu, G. Wang, *Mater. Chem. Front.* **2021**, *5*, 3735.
[14] X. Gao, X. Zhang, X. Liu, Y. Tian, Q. Cai, M. Jia, X. Yan, *Small Methods* **2023**, *7*, 2300152.
[15] D. Bérardan, S. Franger, A. K. Meena, N. Dragoe, *J. Mater. Chem. A* **2016**, *4*, 9536.

[16] Y. Xu, X. Xu, L. Bi, *J. Adv. Ceram.* **2022**, *11*, 794.
[17] Y. Sun, S. Dai, *Sci. Adv.* **2021**, *7*, eabg1600.
[18] C. M. Rost, E. Sachet, T. Borman, A. Moballegh, E. C. Dickey, D. Hou, J. L. Jones, S. Curtarolo, J.-P. Maria, *Nat. Commun.* **2015**, *6*, 8485.
[19] P. K. Davies, A. Navrotsky, *J. Solid State Chem.* **1981**, *38*, 264.
[20] M. Brahlek, M. Gazda, V. Keppens, A. R. Mazza, S. J. Mccormack, A. Mielewczyk-Gryn, B. Musico, K. Page, C. M. Rost, S. B. Sinnott, C. Toher, T. Z. Ward, A. Yamamoto, *APL Mater.* **2022**, *10*, 110902.
[21] A. Salian, S. Mandal, *Crit. Rev. Solid State Mater. Sci.* **2021**, *47*, 142.
[22] A. Amiri, R. Shahbazian-Yassar, *J. Mater. Chem. A* **2021**, *9*, 782.
[23] M. Mozdzierz, J. Dabrowa, A. Stepien, M. Zajusz, M. Stygar, W. Zajac, M. Danielewski, K. Swierczek, *Acta Mater.* **2021**, *208*, 116735.
[24] M. Balcerzak, K. Kawamura, R. Bobrowski, P. Rutkowski, T. Brylewski, *J. Electron. Mater.* **2019**, *48*, 7105.
[25] A. D. Dupuy, J. M. Schoenung, *Mater. Charact.* **2022**, *193*, 112301.
[26] A. D. Dupuy, I.-T. Chiu, P. Shafer, E. Arenholz, Y. Takamura, J. M. Schoenung, *J. Eur. Ceram. Soc.* **2021**, *41*, 6660.
[27] H. Vahidi, K. Syed, H. Guo, X. Wang, J. L. Wardini, J. Martinez, W. J. Bowman, *Crystals* **2021**, *11*, 878.
[28] J. Lee, D. S. Chung, *J. Mater. Chem. C* **2023**, *11*, 5241.
[29] G. F. Harrington, D. Kalaev, B. Yildiz, K. Sasaki, N. H. Perry, H. L. Tuller, *ACS Appl. Mater. Interfaces* **2019**, *11*, 34841.
[30] T. Lee, J. Qi, C. A. Gadre, H. Huyan, S.-T. Ko, Y. Zuo, C. Du, J. Li, T. Aoki, R. Wu, J. Luo, S. P. Ong, X. Pan, *Nat. Commun.* **2023**, *14*, 1940.
[31] S.-T. Ko, T. Lee, J. Qi, D. Zhang, W.-T. Peng, X. Wang, W.-C. Tsai, S. Sun, Z. Wang, W. J. Bowman, S. P. Ong, X. Pan, J. Luo, *Matter* **2023**, *6*, 2395.
[32] X. Tong, W. J. Bowman, A. Mejia-Giraldo, P. A. Crozier, D. S. Mebane, *J. Phys. Chem. C* **2020**, *124*, 23619.
[33] W. J. Bowman, J. Zhu, R. Sharma, P. A. Crozier, *Solid State Ion.* **2015**, *272*, 9.
[34] W. J. Bowman, M. N. Kelly, G. S. Rohrer, C. A. Hernandez, P. A. Crozier, *Nanoscale* **2017**, *9*, 17293.
[35] W. J. Bowman, A. Darbal, P. A. Crozier, *ACS Appl. Mater. Interfaces* **2020**, *12*, 507.
[36] K. Syed, M. Xu, K. K. Ohtaki, D. Kok, K. K. Karandikar, O. A. Graeve, W. J. Bowman, M. L. Mecartney, *Materialia* **2020**, *14*, 100890.
[37] D. Berardan, A. K. Meena, S. Franger, C. Herrero, N. Dragoe, *J. Alloys Compd.* **2017**, *704*, 693.
[38] M. C. M. O'brien, C. C. Chancey, *Am. J. Phys.* **1993**, *61*, 688.
[39] X. Guo, W. Sigle, J. Maier, *J. Am. Ceram. Soc.* **2003**, *86*, 77.
[40] A. D. Dupuy, M. R. Chellali, H. Hahn, J. M. Schoenung, *J. Mater. Res.* **2022**.
[41] D. A. Porter, K. E. Easterling, K. E. Easterling, *Phase Transformations in Metals and Alloys (Revised Reprint)*, 3rd ed., CRC Press, Boca Raton, FL, USA, **2009**.
[42] J. L. Lensch-Falk, J. D. Sugar, M. A. Hekmaty, D. L. Medlin, *J. Alloys Compd.* **2010**, *504*, 37.
[43] R. Jungblut, M. T. Johnson, J. aan de Stegge, A. Reinders, F. J. A. den Broeder, *J. Appl. Phys.* **1994**, *75*, 6424.
[44] J. Kim, S. J. Hong, J. K. Lee, K. B. Kim, J. H. Lee, J. Han, C. Lee, G. Song, *Mater. Sci. Eng. A* **2021**, *823*, 141763.
[45] A. J. Ardell, V. Ozolins, *Nat. Mater.* **2005**, *4*, 309.
[46] Z. Grzesik, G. Smola, M. Stygar, J. Dabrowa, M. Zajusz, K. Mroczka, M. Danielewski, *J. Eur. Ceram. Soc.* **2019**, *39*, 4292.
[47] E. Hristova, R. Janisch, R. Drautz, A. Hartmaier, *Comput. Mater. Sci.* **2011**, *50*, 1088.
[48] E. K. Akdogan, I. Şavklıyıldız, B. Berke, Z. Zhong, L. Wang, D. Weidner, M. C. Croft, T. Tsakalakos, *J. Appl. Phys.* **2012**, *111*, 053506.
[49] H.-B. Zhou, S. Jin, Y. Zhang, G.-H. Lu, F. Liu, *Phys. Rev. Lett.* **2012**, *109*, 135502.
[50] S. Chae, L. Williams, J. Lee, J. T. Heron, E. Kioupakis, *NPJ Comput. Mater.* **2022**, *8*, 95.
[51] N. Osenciat, D. Bérardan, D. Dragoe, B. Léridon, S. Holé, A. K. Meena, S. Franger, N. Dragoe, *J. Am. Ceram. Soc.* **2019**, *102*, 6156.
[52] T. J. Lewis, A. J. Wright, *J. Phys. Appl. Phys.* **1968**, *1*, 441.
[53] I. Singh, R. K. Bedi, *Appl. Surf. Sci.* **2011**, *257*, 7592.
[54] M. Younas, M. Nadeem, M. Idrees, M. J. Akhtar, *Appl. Phys. Lett.* **2012**, *100*, 152103.
[55] F. Lange, M. Martin, *Berichte Bunsenges. Für Phys. Chem.* **1997**, *101*, 176.
[56] S. P. Mitoff, *J. Chem. Phys.* **2004**, *35*, 882.
[57] L. Qiao, X. Bi, *Europhys. Lett.* **2011**, *93*, 57002.
[58] H. Wang, C. Li, H. Zhao, R. Li, J. Liu, *Powder Technol.* **2013**, *239*, 266.
[59] L. Sun, X. Huang, L. Wang, A. Janotti, *Phys. Rev. B* **2017**, *95*, 245101.
[60] M. Biesuz, L. Spiridigliozzi, G. Dell'agli, M. Bortolotti, V. M. Sglavo, *J. Mater. Sci.* **2018**, *53*, 8074.
[61] V. Jacobson, J. Huang, C. J. Titus, R. W. Smaha, M. Papac, S. J. Lee, A. Zakutayev, G. L. Brennecka, *J. Am. Ceram. Soc.* **2023**, *106*, 1531.
[62] *Introduction to Focused Ion Beams: Instrumentation, Theory, Techniques and Practice* (Eds: L. A. Giannuzzi, F. A. Stevie), Springer US, Boston, MA, **2005**.
[63] G. Kresse, J. Furthmüller, *Phys. Rev. B* **1996**, *54*, 11169.
[64] G. Kresse, J. Furthmüller, *Comput. Mater. Sci.* **1996**, *6*, 15.
[65] R. Janisch, C. Elsässer, *Phys. Rev. B* **2003**, *67*, 224101.
[66] S. L. Dudarev, G. A. Botton, S. Y. Savrasov, C. J. Humphreys, A. P. Sutton, *Phys. Rev. B* **1998**, *57*, 1505.
[67] P. E. Blöchl, *Phys. Rev. B* **1994**, *50*, 17953.
[68] G. Kresse, D. Joubert, *Phys. Rev. B* **1999**, *59*, 1758.
[69] H. J. Monkhorst, J. D. Pack, *Phys. Rev. B* **1976**, *13*, 5188.
[70] X. Zhou, D. Marchand, D. L. Mcdowell, T. Zhu, J. Song, *Phys. Rev. Lett.* **2016**, *116*, 075502.
[71] S. Wang, T. Kobayashi, M. Dokiya, T. Hashimoto, *J. Electrochem. Soc.* **2000**, *147*, 3606.
[72] S. Kikuchi, H. Oda, S. Kiyohara, T. Mizoguchi, *Phys. B Condens. Matter* **2018**, *532*, 24.
[73] Y. Xia, Z. Wang, L. Wang, Y. Chen, Z. Liu, Q. Wang, L. Wu, H. Deng, *Metals* **2022**, *12*, 763.
[74] P. Hirel, G. F. B. Moladje, P. Carrez, P. Cordier, *Phys. Chem. Miner.* **2019**, *46*, 37.